URTeC: 2875453

Induced Seismicity Near Fox Creek, Alberta: Interpretation of Source Mechanisms

Hongliang Zhang*[1], David W. Eaton[1]; 1. Department of Geoscience, University of Calgary.

Abstract

Shallow borehole microseismic monitoring was undertaken during multi-stage hydraulic fracturing operations near Fox Creek, Alberta. P-wave focal-mechanism inversion was applied to 17 events with magnitudes greater than *M* 1.5 by fitting P-wave polarities and 3C amplitudes. By analyzing the inverted source mechanisms, the 17 induced events can be classified into two main groups. Group one consists of N-S (or E-W) trending strike-slip earthquakes, while group two consists of NE-SW or NW-SE trending oblique slip events. In the case of group one, decomposition of the source mechanisms shows that they are dominated by double-couple components (typically >75%). In the case of group two, source mechanisms exhibit significant non-double-couple components, consistent with minor tensile opening/closing or complex fault geometry. The latter might include multiple intersecting fractures, dilatant jogs created at the overlapping areas of multiple fractures, or non-planar fault geometry.

Introduction

Understanding source mechanisms of induced earthquakes is important to distinguish them from natural earthquakes and to estimate time-dependent seismic hazard in areas where large-scale fluid injection is ongoing (Zhang et al., 2016). In general, conventional source-mechanism inversion methods can be classified into three main categories: P-wave first motion-based methods (Reasenberg and Oppenheime, 1985; Hardebeck and Shearer, 2002), P-wave and/or S-wave amplitude-based methods (Rau et al., 1996; Nakamura et al., 1999) and waveform-based methods (e.g., Sipkin, 1986; Zhu and Helmberger, 1996).

The present study is located west of Fox Creek, Alberta, within a region where a sharp increase in the frequency of injection-induced seismicity has occurred since December 2013 (Schultz et al., 2018). In contrast to the central United States where saltwater disposal is inferred to be the dominant triggering mechanism of induced earthquakes, hydraulic fracturing is thought to be the dominant, albeit infrequent, triggering mechanism in the Western Canada Sedimentary Basin (Atkinson et al., 2016, Bao and Eaton, 2016). Investigations of source mechanisms for the induced earthquakes near the Fox Creek area are documented in previous studies (e.g., Eaton and Mahani, 2015; Zhang et al., 2016; Wang et al., 2016; Wang et al., 2017); however, most of these works are based on relatively sparse regional seismic networks that have a magnitude detection threshold that is generally greater than *M* 2.0.

In this study, we undertake a detailed investigation of 17 earthquakes with magnitudes larger than *M* 1.5 that occurred between November 10 and November 29, 2016. All of the events occurred during a multi-well hydraulic-fracturing completions program west of Fox Creek, Alberta. This study extends previous induced-seismicity investigations in this area through the use of a dense shallow-well array to investigate an extended sequence of events. We begin by introducing the dataset and then we outline our focal-mechanism inversion and moment-tensor inversion approaches. Finally, comparisons between inverted focal mechanisms and moment-tensor solutions are made to provide further insights into the geomechanical significance of the events.

Method

Focal-mechanism solutions were obtained to estimate source mechanisms using the polarities of observed P-wave first motions. Polarities were picked on the vertical component, which for our dataset usually has the highest-amplitude response for P-wave arrivals compared with the horizontal components. The focal mechanism was then computed by minimizing the misfit between predicted and observed polarities using a grid search algorithm, in which all the possible strike, dip, rake angles were considered with a sampling of 2° for each. The following objective function is used to evaluate each trial focal mechanism:

$$E = \sum_{i=1}^{M} [Pol^{obs}(i) - Pol^{mod}(i)]^2 , \quad (1)$$

where Pol^{obs} and Pol^{mod} are the picked and modeled polarities (1 = positive and -1 = negative), and M is the total number of receivers. The modeled polarities were calculated based on the P-wave radiation pattern of a double-couple source (Stein and Wysession, 2003).

We performed the moment-tensor inversion based on the 3C amplitudes of direct P-wave in a 1-D layered isotropic medium. For a homogeneous region around a source located at the origin, the ith component of particle motion arising from the radiated P-wave can be represented as (Aki and Richards, 2002):

$$u_i^P(x,t) = (4\pi r \rho \alpha^3)^{-1} \{\gamma_i \gamma_j \gamma_k M_{jk}\} \cdot \omega(t - \tau_P) , \quad (2)$$

where r denotes the source-receiver distance; ρ and α are density and P-wave velocity; γ_i is the direction cosine at the source of the ray to the receiver; $\omega(t)$ is the displacement time function at the source, τ_P is the travel time from source to receiver, and the dot notion denotes time derivative. Terms within the curly braces represent the P-wave radiation pattern, and the summation convention is used in this equation. In addition, for a 1-D layered velocity model, ρ represents the average density, while r and α denote the distance and average P-wave velocity along the raypath, respectively.

Based on equation (2), the observed 3C ground displacement amplitudes of direction P-wave can be cast in matrix notation as

$$\mathbf{d}^{obs} = \mathbf{G}\mathbf{m} + \mathbf{n} . \quad (3)$$

The least-squares solution to this overdetermined problem is given by:

$$\hat{\mathbf{m}} = (\mathbf{G}^T\mathbf{G})^{-1}\mathbf{G}^T\mathbf{d}^{obs} . \quad (4)$$

Dataset

The study area as shown in Figure 1 is situated west of Fox Creek, Alberta. Microseismic monitoring was carried out to record continuous ground-motion data between October 25 and November 29, 2016 over a four-well hydraulic fracturing treatment. The recording system consisted of a strong-motion accelerometer, six broadband seismometers and an array of 69 shallow borehole geophone system and two surface three-component geophones. In terms of the shallow borehole systems, each is comprised of three one-component geophones and one three-component geophone. In this study, only the 68 three-component geophones (marked in black triangles in Figure 1) were used. This distribution of stations provides good azimuthal coverage for the moment tensor calculations. As marked by circles in Figure 2, 17 induced events with magnitude larger than M 1.5 were observed during the monitoring period. Table 1 shows the origin times and event magnitudes reported on a regional event catalog. In this study, the 17 events were located using P-wave arrival times based on the velocity model derived from the available nearby well log data.

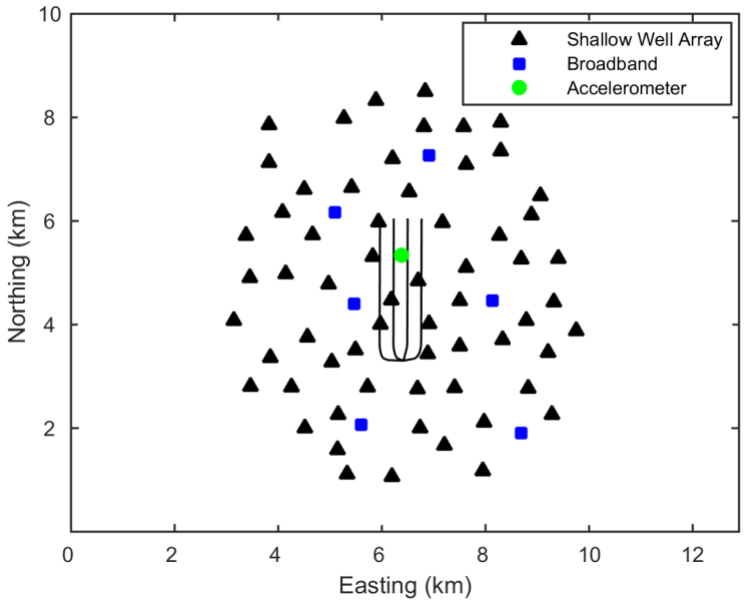

Figure 1: Map view of locations of horizontal wells (black lines), shallow borehole geophones (black triangles) and broadband seismometers (blue squares) and the accelerometer (green dot) used in this study.

Table 1: Catalog of 17 induced events reported on a regional monitoring network.

Event ID	Date and Time (UTC)	Reported Magnitude
1	2016/11/10 03:05:55	M_W 3.1
2	2016/11/10 09:55:29	M_W 2.8
3	2016/11/11 02:33:46	M_W 2.6
4	2016/11/11 11:24:09	M_W 2.8
5	2016/11/15 13:28:11	MI 1.59
6	2016/11/21 21:39:45	MI 1.84
7	2016/11/22 10:04:31	MI 2.1
8	2016/11/22 11:21:06	MI 1.5
9	2016/11/22 13:18:44	MI 1.68
10	2016/11/22 18:18:25	M_W 2.6
11	2016/11/25 05:31:25	M_W 3.4
12	2016/11/25 21:24:01	M_W 3.5
13	2016/11/27 14:52:51	M_W 2.8
14	2016/11/28 06:53:38	M_W 3
15	2016/11/28 15:35:27	MI 1.86
16	2016/11/29 04:12:48	M_W 3
17	2016/11/29 10:15:25	M_W 3.6

Results

Table 2 shows the focal-mechanism-inversion results based on P-wave polarities as well as the moment-tensor-inversion results based on 3C displacement amplitudes of direct P-wave. The mechanisms are presented in the table as beach ball diagrams. For some events, a set of focal mechanism solutions were obtained that fit the observed polarities equally well, and a representative nodal plane is shown with color fill in Table 2. In general, however, there are two dominant focal mechanisms within the 17 induced events. Events 1-6 and 11-17 share a similar strike-

slip focal mechanism with high dip angles typically >85°. The two nodal planes for this group strike N-S and E-W. For events 7-10, the two nodal planes of the focal mechanism exhibit either NE-SW trending strike-dips with dip angles between 45° and 60° or NW-SE trending strike-slips with high dip angles (typically >85°) accompanied by significant strike-slip component.

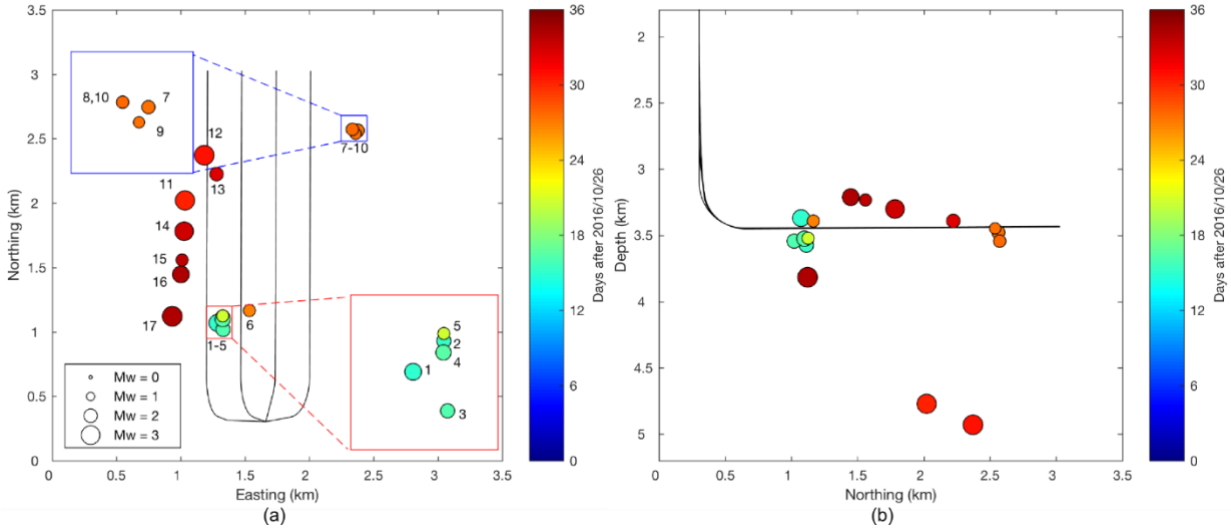

Figure 2: (a) Map view and (b) side view of locations of 17 induced earthquakes investigated in this study. Event symbols are scaled based on moment magnitude and are colored by the date of occurrence.

Similarly, the moment-tensor-inversion results also exhibit two groups of source mechanisms: group one with events 1-6, 11-17 and group two with events 7-10. For group one, the nodal planes the best-fitting DC mechanism are very close to the previously described focal-mechanism-inversion results of this group. On the other hand, for group two, the nodal planes of the best-fitting DC solutions differ from the focal-mechanism solutions. This difference occurs because the moment-tensor solution has additional degrees of freedom that include non-DC components.
Source parameters resulting from the moment-tensor inversion are summarized in Table 3. The seismic moment magnitudes were estimated by fitting Brune model (Brune, 1970; Brune, 1971), resulting in magnitudes ranging between M_W 1.55 and M_W 3.22. The misfits between the observed and theoretical P-wave amplitudes are relatively small, with misfits of <15% for most of events.

The moment tensors can also be represented graphically using a Hudson diagram (Hudson et al., 1989). This plot is parameterized using *T*, describing the deviatoric part of the moment tensor, ranging from -1 to 1 from the left to the right side of the plot, and with the parameter *k* measuring the volume change ranging from -1 at the bottom of the plot to 1 at the top. The DC region is situated in the middle of the plot. In Figure 3, it can be observed that the 4 events in the second group exhibit significant larger non-DC components compared with the 13 events in group one. Figure 4 shows the percentage of each component after the complete moment-tensor decomposition for each of the 17 events. For events 1-6 and 11-17, the focal mechanism is dominated by the DC (typically >75%) accompanied by minor CLVD and ISO. However, for events 7-10, significant non-DC components (up to 62%) are observed, which needs further interpretation.

Table 2: Summary of best-fitting focal-mechanism solutions and moment-tensor solutions.

Event ID	Focal Mechanism	Moment Tensor	Event ID	Focal Mechanism	Moment Tensor	Event ID	Focal Mechanism	Moment Tensor
1	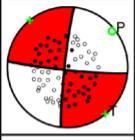	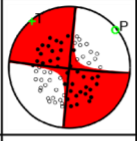	2		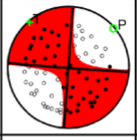	3	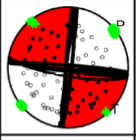	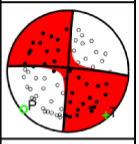
4		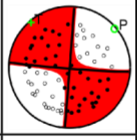	5	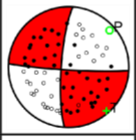	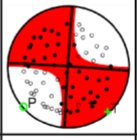	6	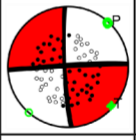	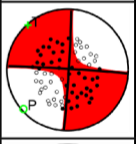
7		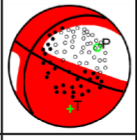	8	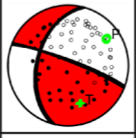	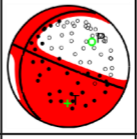	9		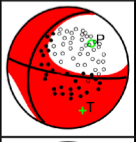
10	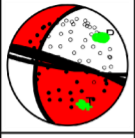	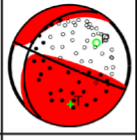	11	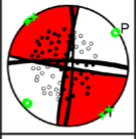	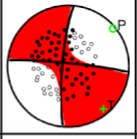	12	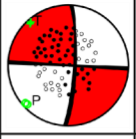	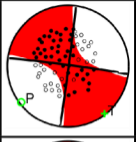
13	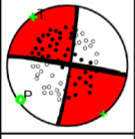	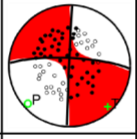	14	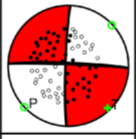	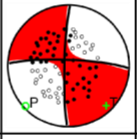	15		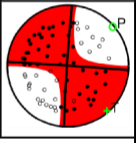
16	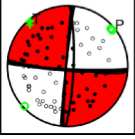	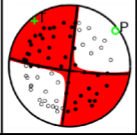	17	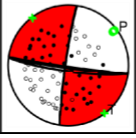	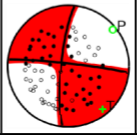			

Table 3: Source parameters retrieved from moment-tensor inversion.

Event ID	Moment Magnitude (M_w)	Misfit (%)	Fault Planes for best DC (strike, dip, rake)
1	2.67	11.6	(186, 90, -178) (96, 88, 0)
2	2.15	8.7	(4, 90, 179) (94, 89, 0)
3	2.14	8.6	(185, 90, 175) (275, 85, 0)
4	2.37	7.4	(4, 90, 178) (94, 88, 0)
5	1.75	7.1	(184, 89, 179) (274, 89, 1)
6	1.75	11.1	(4, 88, -179) (273, 89, -2)
7	1.94	12.3	(115, 82, -58) (217, 33, -166)
8	1.55	10.8	(112, 88, -67) (207, 23, -174)
9	1.59	17.6	(99, 80, -53) (202, 38, -164)
10	1.82	10.2	(113, 87, -61) (208, 29, -175)
11	3.12	13.1	(185, 82, 176) (276, 86, 8)
12	3.20	16.4	(8, 89, -178) (278, 88, -1)
13	2.01	17.6	(182, 89, 169) (273, 79, 1)
14	3.00	18.6	(181, 84, 172) (272, 82, 6)
15	1.76	7.6	(184, 89, 180) (274, 90, 1)
16	2.65	13.6	(7, 89, 173) (97, 83, 1)
17	3.22	11.0	(186, 80, 176) (276, 86, 10)

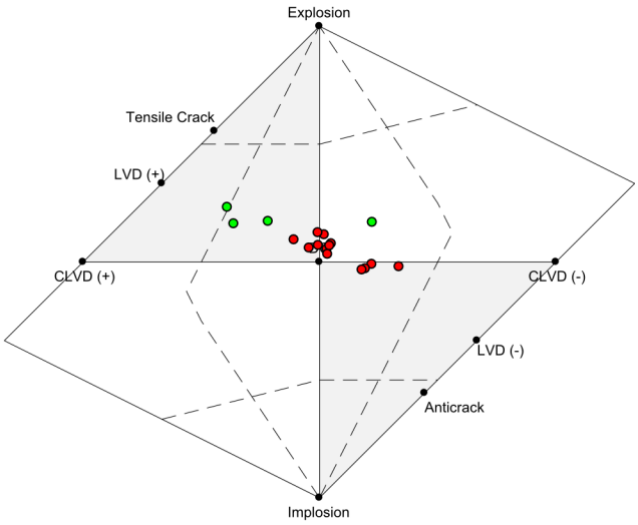

Figure 3: Hudson diagram showing mechanisms for the 17 induced events. Events within group one are marked by red dots, and events within group two are marked by green dots. Double-couple (DC) events plot in the middle of the diagram. (C)LVD denotes (compensated) linear vector dipole.

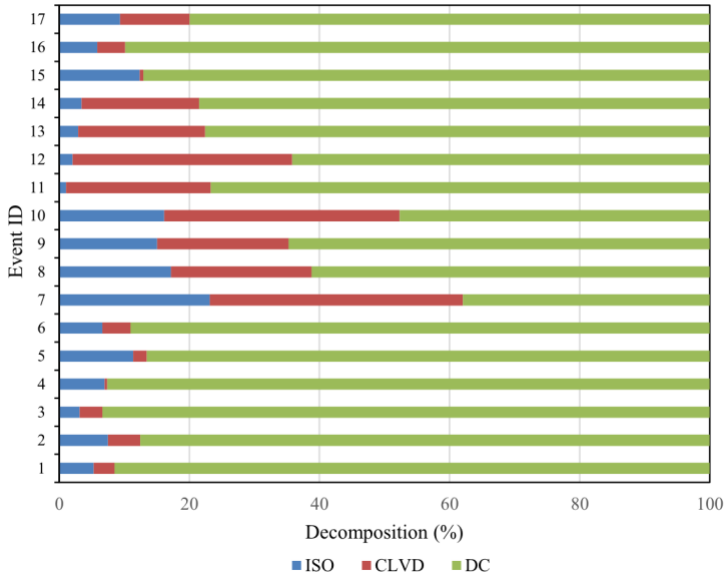

Figure 4: Decomposition of the moment tensor into double-couple (DC, green), compensated linear vector dipole (CLVD, red), and isotropic components (ISO, blue) calculated for each event.

Discussion

The estimated moment magnitudes for the 17 induced events in this study range between M_W 1.55 and M_W 3.22, which are slightly lower than the reported values on the regional catalog (Table 1). As shown in Figure 2, focal depths of these events vary from 3211 m to 4929 m, and most of them are in vicinity of the fluid injection depth (~3.4 km) of hydraulic fracturing treatments. However, for events 11 and 12, compared with other events, they exhibit slightly deeper focal depth (> 4 km), which lies in the Precambrian crystalline basement (~3.8 km according to Pilkington et al., 2000; Majorowicz et al, 2014; Wang et al., 2017). Nevertheless, the relatively shallow focal depth of these events exhibits a good agreement with previous studies (Zhang et al., 2016; Wang et al., 2016; Wang

et al., 2017), in which the focal depths of the hydraulic-fracturing induced earthquakes in this area are typically less than 5 km.

Our focal mechanism solutions for both group one and group two are consistent with previous studies in the nearby area (Eaton and Mahani, 2015; Wang et al., 2017; Zhang et al., 2016), in which the source mechanisms yield either N-S/E-W or NE-SW/NW-SE trending nodal planes. However, relative to group one which exhibits strike-slip mechanism with nearly vertical N-S/E-W nodal planes as well as minor non-DC components (typically < 25%), significant dip-slip components (for the NW-SE trending nodal plane) and small dip angles (< 40° for the NE-SW trending nodal plane) are observed within the best DC solutions of group two. In addition, significant non-DC (up to 62%) are also observed in the moment-tensor solutions for group two. The non-DC component can be interpreted in various ways. In the context of hydraulic fracturing, volumetric components of the moment tensor could signify a component of tensile opening. On the other hand, non-DC components can also arise from complex source characteristics such as multiple intersecting fractures, dilatant jogs created at the overlapping areas of multiple fractures, or non-planar fault geometry (Zhang et al., 2016).

Moment-tensor inversion results may contain artifacts due to a number of factors, such as the S/N for a given dataset, uncalibrated velocity model, anisotropy of velocity model, source location errors and errors in amplitude picks, and inversion algorithm itself (Zhang et al., 2016). Future work is needed to determine the possible effects from these sources of artifacts.

Conclusions

The P-wave polarity-based focal-mechanism inversion and P-wave amplitude-based moment-tensor inversion were undertaken for a set of 17 induced events recorded during a hydraulic fracturing program west of Fox Creek, Alberta. The moment magnitudes of these events are estimated to range between M_W 1.55 and M_W 3.22. In both of two sets of inversion results, two groups of source mechanisms were identified: group one, predominantly double-couple (DC) N-S or E-W trending strike-slip events; and group two, a set of events exhibiting significant non-DC components with high-dip angle dip-slip (thrust-faulting) or low-dip angle strike-slip. For group one, the nodal planes of the best-fitting DC within the moment tensor are very close to the focal-mechanism-inversion results. For the other group, the nodal plane solutions exhibit slightly larger difference between the two sets of results. The full moment tensors are decomposed into three components: ISO, DC and CLVD. The 13 events within group one have DC-dominated source mechanisms (typically > 75%), accompanied by minor CLVD and ISO. For the 4 events within group two, significant non-DC components are observed (up to 62%).

Acknowledgements

Two anonymous companies are thanked for providing access to the data of shallow wellbore array. The BuriedArray acquisition method was used under license from Microseismic Inc. This work was supported by the Natural Sciences and Engineering Research Council of Canada (NSERC) through the NSERC/Chevron Industrial Research Chair in Microseismic System Dynamics and a Collaborative Research and Development (CRD) grant. The CRD grant is also supported by TransAlta Utilities and Nanometrics Ltd. Sponsors of the Microseismic Industry Consortium are also thanked for their ongoing support. Mitacs is thanked for the financial support through Mitacs-Accelerate Graduate Research Internship Program. The event catalog in Table 1 was taken from the TA regional seismic catalog maintained by Nanometrics.

References

Aki, K., and P. G. Richards, 2002, Quantitative Seismology: University Science Books.

Bao, X., and D. W. Eaton, 2016, Fault activation by hydraulic fracturing in western Canada: Science, 354, 1406-1409.

Atkinson, G. M., D. W. Eaton, H. Ghofrani, D. Walker, B. Cheadle, R. Schultz, R. Shcherbakov, K. Tiampo, J. Gu, R. M. Harrington, Y. Liu, M. van der Baan, and H. Kao, 2016, Hydraulic fracturing and seismicity in the Western Canada Sedimentary Basin: Seismological Research Letters, 87(3), 631-647.

Brune, J. N., 1970, Tectonic stress and the spectra of seismic shear waves from earthquakes: Journal of Geophysical Research, 75, 4997-5009.

Brune, J. N., 1971, Correction: Journal of Geophysical Research, 76, 5002.

Eaton, D. W., and A. B. Mahani, 2015, Focal mechanisms of some inferred induced earthquakes in Alberta, Canada: Seismological Research Letters, 86(4), 1078-1085.

Hardebeck, J. L., and P. M. Shearer, 2002, A new method for determining first-motion focal mechanisms: Bulletin of the Seismological of Society of America, 92(6), 2264-2276.

Hudson, J. A., R. G. Pearce, and R. M. Rogers, 1989, Source type plot or inversion of the moment tensor: Journal of Geophysical Research, 94(B1), 765-774.

Majorowicz, J, J. Chan, J. Crowell, W. Gosnold, L. M. Heaman, J. Kück, G. Nieuwenhuis, D. R. Schimitt, M. Unsworth, N. Walsh, and S. Weides, 2014, The first deep heat flow determination in crystalline basement rocks beneath the Western Canadian Sedimentary Basin: Geophysical Journal International, 197(2), 731-747.

Nakamura, A., S. Horiuchi, and A. Hasegawa, 1999, Joint focal mechanism determination with source-region station corrections using short-period body-wave amplitude data: Bulletin of the Seismological of Society of America, 89(2), 373-383.

Pilkington, M., W. F. Miles, G. M. Ross, and W. R. Roest, 2000, Potential-field signatures of buried Precambrian basement in the Western Canada Sedimentary Basin: Canadian Journal of Earth Sciences, 37, 1453-1471.

Rau, R., F. T.Wu, and T. Shin, 1996, Regional network focal mechanism determination using 3D velocity model and SH/P amplitude ratio: Bulletin of the Seismological of Society of America, 86(5), 1270-1283.

Reasenberg, P., and D. Oppenheimer, 1985, FPFIT, FPPLOT, and FPPAGE: FORTRAN computer programs for calculating and displaying earthquake fault-plane solutions: U.S. Geological Survey Open-File Report, 85-739, 109.

Schultz, R., G. Atkinson, D. W. Eaton, Y. J. Gu, and H. Kao, 2018, Hydraulic fracturing volume is associated with induced earthquake productivity in the Duvernay play: Science, 359, 304-308.

Sipkin, S. A., 1986, Estimation of earthquake source parameters by the inversion of waveform data: Global seismicity, 1981-1983: Bulletin of the Seismological of Society of America, 76(6), 1515-1541.

Stein, S., and M. Wysession, 2003, An introduction to seismology, earthquakes, and earth structure: Blackwell Publishing.

Wang, R., Y. J. Gu, R. Schultz, A. Kim, and G. Atkinson, 2016, Source analysis of a potential hydraulic-fracturing-induced earthquake near Fox Creek, Alberta: Geophysical Research Letters, 43, 564-573.

Wang, R., Y. J. Gu, R. Schultz, M. Zhang and A. Kim, 2017, Source characteristics and geological implications of the January 2016 induced earthquakes swarm near Crooked Lake, Alberta: Geophysical Journal International, 210, 979-988.

Zhang, H., D. W. Eaton, G. Li, Y. Liu, and R. M. Harrington, 2016, Discriminating induced seismicity from natural earthquakes using moment tensors and source spectra: Journal of Geophysical Research, 121(2), 972-993.

Zhu, L., and D. V. Helmberger, 1996, Advancement in source estimation techniques using broadband regional seismograms: Bulletin of the Seismological of Society of America, 86(5), 1634-1641.